



HAL
open science

Magma interactions, crystal mush formation, timescales, and unrest during caldera collapse and lateral eruption at ocean island basaltic volcanoes (Piton de la Fournaise, La Réunion)

H. Albert, F. Costa, A. Di Muro, J. Herrin, N. Métrich, E. Deloule

► **To cite this version:**

H. Albert, F. Costa, A. Di Muro, J. Herrin, N. Métrich, et al.. Magma interactions, crystal mush formation, timescales, and unrest during caldera collapse and lateral eruption at ocean island basaltic volcanoes (Piton de la Fournaise, La Réunion). *Earth and Planetary Science Letters*, 2019, 515, pp.187-199. 10.1016/j.epsl.2019.02.035 . insu-03586645

HAL Id: insu-03586645

<https://insu.hal.science/insu-03586645>

Submitted on 28 Feb 2022

HAL is a multi-disciplinary open access archive for the deposit and dissemination of scientific research documents, whether they are published or not. The documents may come from teaching and research institutions in France or abroad, or from public or private research centers.

L'archive ouverte pluridisciplinaire **HAL**, est destinée au dépôt et à la diffusion de documents scientifiques de niveau recherche, publiés ou non, émanant des établissements d'enseignement et de recherche français ou étrangers, des laboratoires publics ou privés.



Distributed under a Creative Commons Attribution 4.0 International License



Magma interactions, crystal mush formation, timescales, and unrest during caldera collapse and lateral eruption at ocean island basaltic volcanoes (Piton de la Fournaise, La Réunion)

H. Albert ^{a,b,*}, F. Costa ^{a,b}, A. Di Muro ^c, J. Herrin ^a, N. Métrich ^c, E. Deloule ^d

^a Earth Observatory of Singapore, Nanyang Technological University, Singapore

^b Asian School of the Environment, Nanyang Technological University, Singapore

^c Institut De Physique Du Globe De Paris, Sorbonne Paris-Cité, Université Paris Diderot, UMR 7154 CNRS, Paris, France

^d Centre de Recherches Pétrographiques et Géochimiques, Nancy-Université, France

ARTICLE INFO

Article history:

Received 22 June 2018

Received in revised form 25 February 2019

Accepted 27 February 2019

Available online 2 April 2019

Editor: T.A. Mather

Keywords:

olivine
caldera
melt inclusion
diffusion
timescales
crystal mush

ABSTRACT

The dynamics of magmatic processes at large mafic ocean island volcanoes control the likely locations (central caldera versus flanks) and timing of their eruptions. Crystals and their melt inclusions are key witnesses of these processes but are rarely studied in detail and in the same samples. Here we report the crystal and melt inclusion compositions of the April 2007 caldera-forming eruption of Piton de la Fournaise volcano and discuss how they relate to geophysical unrest monitoring data. Olivine crystals show mainly normal zoning (decrease in Mg/Fe) towards the rims, and also around some melt inclusions. Many crystals also show fine-scale skeletal structures defined by high phosphorus concentrations. Melt inclusions contain 53–205 ppm CO₂ and 0.25–1.1 wt% H₂O, and δD (δD values expressed as δD_{VSMOW}) ranges from –135 to 62‰. Monitoring data show that inflation of the edifice started about a month before the first 2007 eruption: magma intrusion occurred at ≈ 3 km below sea level, and quickly migrated towards shallower depths (about 1 km above sea level). Such a time frame of magma movement is recorded in the chemical zoning of the olivine crystals that massively and quickly crystallized when reaching shallow depth, without significant interactions between resident and intruding magmas. The intrusion was followed by lateral flank eruption and caldera collapse. The chemical zoning of the olivine crystal rims and around the melt inclusions indicates that the newly created crystal-mush moved laterally towards the surface in matter of days to 3 months. Post-caldera samples show significant H⁺ loss, likely due to the depressurization of the magmatic system stored at shallow level. Our findings are different from other mafic ocean island volcanoes or stratovolcanoes (e.g. Kilauea, Canary Islands, and Etna), where crystals commonly record magma mixing between evolved and shallow melts and intruding mafic melts. We speculate that the difference between our findings and those of similar mafic ocean island volcanoes is due to the variety of magma supply rates from depth.

© 2019 The Author(s). Published by Elsevier B.V. This is an open access article under the CC BY-NC-ND license (<http://creativecommons.org/licenses/by-nc-nd/4.0/>).

1. Introduction

Understanding the processes that occur in the magma plumbing system below ocean island volcanoes and how they relate to monitoring data, are key current topics of research because they can lead to improved volcanic hazard assessment (e.g., Cashman et al., 2017). Crystal compositions and melt inclusions are direct sources of information on the architecture and dynamics of the plumbing system. Crystal zoning patterns can inform us of the

range of magmatic environments, and of the likely processes that lead to eruption (e.g. Albert et al., 2015; Kahl et al., 2011). In the last couple of decades many studies have quantified the timescales of pre-eruptive magmatic processes via combination of diffusion and crystal growth models, in particular using olivine (e.g. Costa et al., 2008; Costa and Dungan, 2005; Shea et al., 2015; Pankhurst et al., 2018). A complementary view of the plumbing system is provided by detailed studies of melt inclusions. The variability of major, trace, and volatile element concentrations of the inclusions also informs us of the heterogeneity and architecture of the system (e.g. Danyushevsky et al., 2004; Métrich et al., 2009; Rasmussen et al., 2018), although the major and volatile element record of melt inclusions can be modified by post-entrapment processes (e.g. Lloyd et al., 2013; Danyushevsky et al., 2000). For rapidly quenched

* Corresponding author at: Earth Observatory of Singapore, Nanyang Technological University, Singapore.

E-mail address: hln.albert@gmail.com (H. Albert).

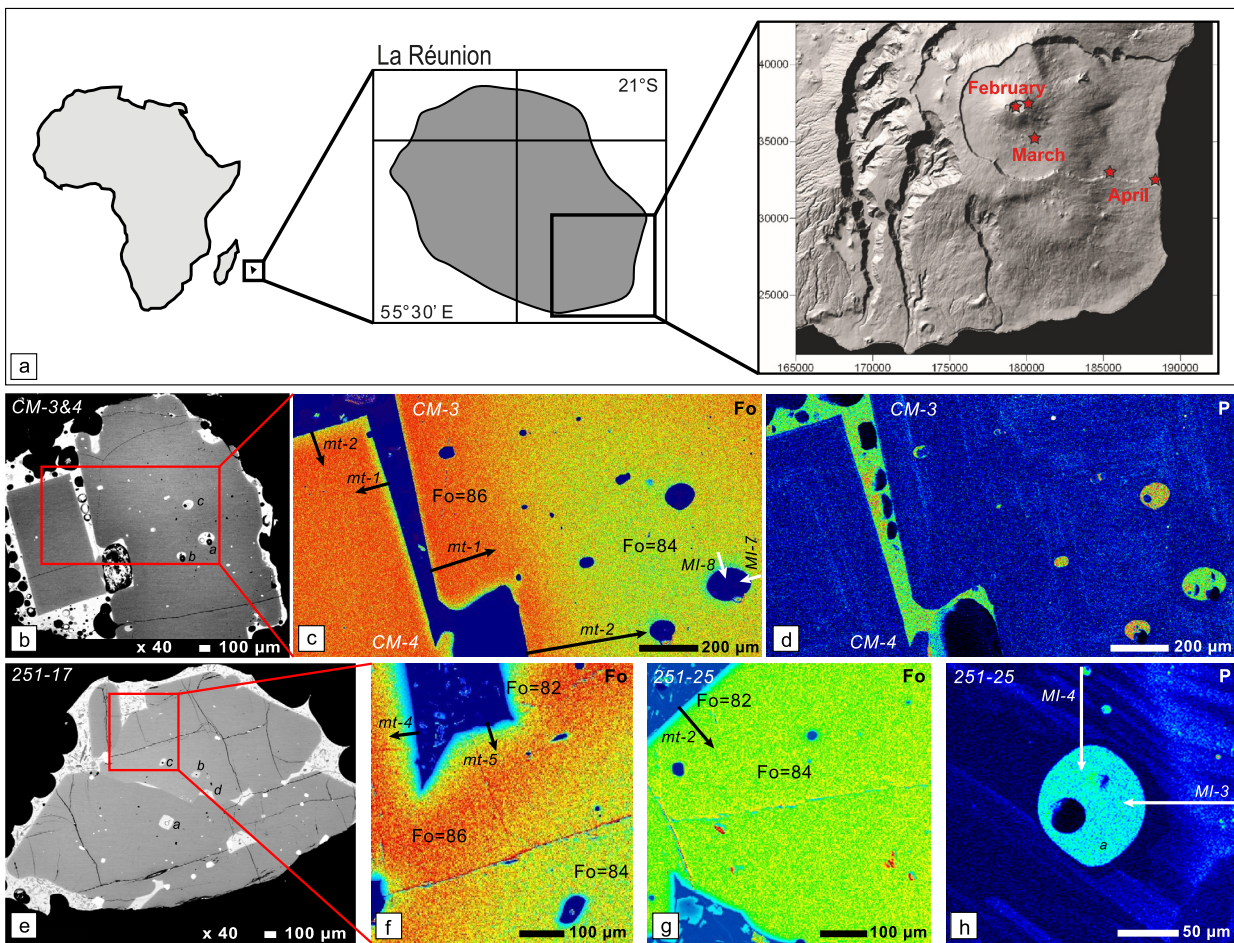


Fig. 1. a) Location of La Réunion Island. The red stars represent the February, March and April 2007 eruptive vents at Piton de la Fournaise. **b–h)** Back-scattered electron (BSE) images, forsterite (Fo), and phosphorous (P) X-Ray compositional maps of representative olivine crystals from the pre-caldera (b–d) and the post-caldera (e–h) samples. In the Fo maps, olivine crystals exhibit weak reverse zoning from core to mantle (from Fo = 84 to Fo = 86) followed by a normal zoning towards the rim (down to Fo = 82). Normal zoning (light blue color in c, f and g) is also observed at the interface between the olivine and the melt inclusions. These observations are common to both samples. Black or white arrows show the location of the electron microprobe traverses and their label; representative compositional profiles are shown in Fig. 2. Letters next to the melt inclusions correspond to those reported in Tables 2 and 3. Panels d) and h) show the complex phosphorous zoning of the olivine with “shadow” P-poor patterns surrounding some of the melt inclusions. (For interpretation of the colors in the figure(s), the reader is referred to the web version of this article.)

samples, the volatile concentrations (H_2O and CO_2) coupled with experimentally calibrated solubility models allows the determination of the volatile saturation pressure, which can be translated into minimum depth of magma storage (Collins et al., 2009; Frezzotti, 2001). Despite the complementary information provided by crystal zoning and the melt inclusions studies, these have rarely been studied together (e.g. Rasmussen et al., 2018; Ruth et al., 2018), and thus we are losing opportunities to obtain a more comprehensive view of the system. Coupling of the depth of magma storage with the times of magma movement allows us to propose links with the eruptive behavior and different phases of eruptions, and especially with the monitoring data describing the unrest preceding the eruptions (Albert et al., 2016, 2015; Kahl et al., 2011; Pankhurst et al., 2018).

The complex dynamics between the central caldera, lateral magma transport, and eruption sites of the April 2018 activity at Kilauea volcano exemplify the need to better understand the plumbing system and the tectonic control of volcanic activity at ocean island volcanoes. Here we investigate the magmatic processes associated with caldera collapse and lateral magma transport recorded in olivine crystals and their melt inclusions on selected samples from the largest historical eruption of Piton de la Fournaise (Michon et al., 2007).

2. Background

2.1. Geological setting

Piton de la Fournaise (PdF) is one of the most active intra-plate basaltic shield volcanoes on Earth (1 eruption every 9 months on average since 1930; Peltier et al., 2009). Collapse of the summit caldera is a rare event, but it occurred in April 2007 during one of its largest eruptions ($\approx 0.15 \text{ km}^3$ of Dense Rock Equivalent; DRE) that lasted 31 days, and led to a ca. 1 km wide \times 0.34 km deep depression due to the summit caldera floor collapse (e.g. Staudacher et al., 2009).

The 2007 eruptions started on the summit of the volcano on February 18th (Fig. 1a). A second small eruption followed on the upper SE flank on March 30th, and from April 2nd until May 1st the eruption moved to lower elevations. The eruption that occurred at low altitude between April and May was the main phase in duration and volume. Previous studies have shown that the bulk-rock composition and crystal content of the erupted magmas changed with time (Di Muro et al., 2014). Aphyric basalt erupted in February and cotectic basalt in March have relatively high Sr isotope ratio ($^{87}\text{Sr}/^{86}\text{Sr} = 0.70420\text{--}0.70418$). Aphyric magmas were also erupted at the beginning of April event, but the crystal content increased rapidly before caldera collapse (olivine basalt) and re-

mained high (oceanite/olivine-rich basalts) after the collapse event until the end of the eruption (more details about crystallinity can be found in Di Muro et al., 2014). The increase in crystal content coincided with a decrease in Sr isotope values ($^{87}\text{Sr}/^{86}\text{Sr} = 0.70412\text{--}0.70418$), with the lowest value measured in a lava erupted just before the summit collapse on April 5th. The evolution in the petrological, chemical and isotopic features of the 2007 lavas and tephra has been attributed to eruption of magmas stored in multiple independent and shallow pockets which were pressurized by a deep input (Di Muro et al., 2014).

2.2. Monitoring data preceding and during the 2007 eruptions

The OVPF (Observatoire Volcanologique du Piton de la Fournaise) has monitored the PdF volcano since 1980, and the 2007 eruption was recorded on a range of monitoring networks, including seismic and geodetic. Long-term precursors of the 2007 eruptions were identified in tilt-signal from a distal station (RER) located on the northern flank of the volcano that showed an inflation-deflation cycle that started on January 2007 and lasted until the end of the eruption in May (Fontaine et al., 2014). This period of inflation has been attributed to a single deep injection of magma (source at ca. 3 km depth below sea level, b.s.l.; Fontaine et al., 2014). Pressurization of the shallow part of the plumbing system following a deep intrusion has also been recently observed in PdF during the 2014–2015 unrest (Peltier et al., 2016).

3. Samples and methods

3.1. Samples description

We use the same samples studied by Di Muro et al. (2014). These include the pre-caldera olivine-basalts (CM labels) erupted between April 2nd and 4th, and post-caldera crystal-rich oceanites (251 labels) emitted near the end of the eruption on April 25th. Oceanites contain up to 60 wt% of olivine phenocrysts ranging from mm to several cm; we have focused on crystals <2 mm. We measured the chemical zoning patterns of a subset of olivine crystals, which were previously studied for their melt inclusion composition and volatile contents (Di Muro et al., 2014). We also report new isotopic analyses of H (values expressed as $\delta\text{D}_{\text{VSMOW}}$) for some of these inclusions. Our new dataset includes the zoning patterns of 13 and 14 olivine crystals from the CM- and 251-samples, respectively, and the δD measurement in 25 melt inclusions.

The pre-caldera samples are cm-size scoria clasts erupted during the initial intense fountaining activity and that should have experienced rapid quenching in air. Post-caldera lava samples (ca. 10 cm large blobs) were taken close to the vent and were quenched in a bucket of water to minimize post-eruptive modifications.

3.2. Analytical methods

We have used standard procedures for the data acquisition and modeling that we summarize below. Further details can be found in the Supplementary Material. The quantitative analyses and the X-ray elemental distribution maps of olivine were obtained using a JEOL JXA 8530F field emission Electron Probe MicroAnalyzer (EPMA). The crystallographic axes were determined by Electron Backscattered Diffraction (EBSD) using a JEOL JSM-7600F equipped with an Oxford/HKL detector and HKL CHANNEL5 software (both at Nanyang Technological University, Singapore). The analytical conditions are detailed in the Supplementary Material and are the same as in Albert et al. (2015).

Major, trace, and volatile (H_2O , CO_2 , S and Cl) element concentrations in melt inclusions have been published in Di Muro

et al. (2014). Water was analyzed by Raman spectroscopy with an argon ion laser, a Labram HR800 spectrometer (ENS-Lyon), and an Olympus microscope. Carbon concentrations and hydrogen isotopic compositions were analyzed using the Cameca IMS1270 ion microprobe at CRPG-CNRS-Nancy. The D/H ratios were determined by measuring the OD^-/OH^- ratios, in monocollection mode with a mass resolution of 15 000 to get a complete separation of $^{16}\text{OH}_2^-$ and ^{16}OD . The hydrogen isotopic compositions of the melt inclusions were acquired following the procedure of Métrich and Deloule (2014) and detailed in the Supplementary Material.

3.3. Modeling

3.3.1. Mg–Fe, Ca, Ni and P diffusion in olivine

Twenty-three rim-to-core, and eight melt inclusion-to-crystal boundary concentration profiles in olivine were obtained for Si, Fe, Mg, Ca, Ni and P (depending on the crystal). We modeled the Fe–Mg, Ni and Ca concentration gradients using the program DIPRA (Girona and Costa, 2013). We apply the anisotropy correction to the results according to equation #5 of Costa and Chakraborty (2004). We report the uncertainty on diffusion times that accounts for analytical and temperature uncertainty as calculated by DIPRA. In addition, DIPRA also calculates a parameter called “discrepancy”, which is basically a goodness of the fit (Girona and Costa, 2013) and which is reported in Table 1. Most of our diffusion times were obtained from fits with a discrepancy of $\leq 10\%$. The temperature and oxygen fugacity ($f\text{O}_2$) used for modeling are $1200 \pm 10^\circ\text{C}$ and 1.2 log units below the NNO buffer for the reverse zoning profiles (pre-caldera samples; labels CM), and $1160 \pm 10^\circ\text{C}$ and 0.8 log units below the NNO buffer for the normal zoning profiles (pre- and post-caldera samples; labels CM and 251). Temperatures have been calculated with the Fo values and the melt inclusions composition by using the olivine-melt equilibrium geothermometer of Helz and Thornber (1987), as described by Di Muro et al. (2014). Oxygen fugacity has been calculated according to Kress and Carmichael (1991). For initial and boundary conditions we used the same as those in Albert et al. (2015) which are detailed in the Supplementary Material. We have also performed a 2-dimensional diffusion model with a finite differences code for one melt inclusion that correlates the anisotropy effect on the chemical diffusion and the data acquired with the X-ray distribution maps. Finally, we have modeled one P compositional profile in the olivine leading up to the olivine-melt inclusion interface. The P traverse has been modeled separately with an initial step-like profile as required by the S-shaped compositional profile.

3.4. H^+ diffusion

The H_2O content of the melt inclusions may vary due to post-entrapment diffusion of H^+ through the host olivine or/and due to degassing (Lloyd et al., 2013; Bucholz et al., 2013; Chen et al., 2011; Gaetani et al., 2012). Thus, it is critical to determine the extent to which melt inclusion data record a variation of entrapment depths versus the partial re-equilibration via dehydration during magma ascent or cooling on the earth’s surface. Here we make use of the H_2O and δD values and attempt to establish the roles of each process.

We have modeled the diffusive re-equilibration of H_2O of eight melt inclusions using the method of Qin et al. (1992), which considers a spherical melt inclusion of radius a hosted in a spherical crystal of radius b , and we report the details of the parameter values and equations used in the calculation in Supplementary Material. Following Di Muro et al. (2014), we have assumed that the largest measured concentrations have not been modified via diffusion and thus we have used them as initial values (e.g. 1–1.3 wt%

Table 1
Timescales (in days) calculated by modeling the chemical diffusion of Fe–Mg, Ni, Ca and P in olivine crystals and at the interface with melt inclusions (MI).

Sample-crystal-MI	Traverse	Elem	P1	P2	B	α	β	γ	Time core	Time Rim/MI ^a	$\Delta(-)$	$\Delta(+)$	Discr. (%)
Crystal core-rim traverse													
CM-2	1	Fo	85.3	86.0	83.6	50	84	45	413	47	48	53	7
CM-2	1	Ni	0.28	0.31	0.21	50	84	45	413	48	55	62	12
CM-2	1	Ca	0.272	0.240	0.295	50	84	45	413	77	49	55	20
CM-2	2	Fo	84.1	85.7	82.8	35	84	55	764	14	81	92	16
CM-2	2	Ni	0.25	0.31	0.26	35	84	55	764	3	88	103	10
CM-2	2	Ca	0.275	0.240	0.326	35	84	55	764	30	84	96	24
CM-3	1	Fo		85.6	83.6	85	15	76	–	45	9	7	14
CM-3	1	Ni		0.29	0.23	85	15	76	–	23	18	8	13
CM-3	1	Ca		0.256	0.308	85	15	76	–	32	17	19	11
CM-3	2	Fo	83.9	85.2	84.2	85	25	65	833	31	90	103	16
CM-3	2	Ni	0.24	0.30	0.25	85	25	65	833	62	131	120	14
CM-3	2	Ca	0.292	0.250	–	85	25	65	833	157	194	180	20
CM-6	1	Fo		85.6	84.3	85	25	65	–	58	10	11	6
CM-6	1	Ni		0.29	0.23	85	25	65	–	23	3	8	9
CM-6	1	Ca		0.250	0.305	85	25	65	–	49	14	17	15
CM-6	2	Fo		85.70	84.53	86	75	15	–	64	9	11	14
CM-6	2	Ni		0.29	0.21	86	75	15	–	47	8	14	8
CM-6	2	Ca		0.250	0.295	86	75	15	–	56	10	13	5
251-17	4	Fo		84.9	82.1	87	3	89	–	37	6	10	<1
251-17	5	Fo		84.8	82.9	86	9	83	–	16	2	5	<1
251-20	3	Fo		84.5	83.5	46	52	67	–	16	5	3	4
251-22	1	Fo		84.6	82.4	3	90	88	–	29	3	6	2
251-25	2	Fo		84.5	81.5	84	43	47	–	9	2	3	1
CM-2-MI-a	6	Fo	84.1		82.4	80	84	11	–	18	3	5	4
CM-3-MI-a	7	Fo	84.2		83.0	85	15	76	–	30	4	22	3
CM-3-MI-a	8	Fo	84.2		82.8	86	75	15	–	23	6	8	1
251-17-MI-a	5	Fo	84.7		83.4	87	35	55	–	2	1	1	2
251-20-MI-a	3	Fo	84.2		83.2	46	52	67	–	7	2	2	1
251-25-MI-a	3	Fo	84.5		83.3	78	83	14	–	8	3	3	<1
251-25-MI-a	3	P	4.9×10^{-3}		6.4×10^{-5}	78	83	14	–	560	78	77	2
251-25-MI-a	4	Fo	84.5		83.5	89	5	85	–	15	3	10	<1

P1 and P2 are the two compositional plateaus observed leading to reverse zoning. B is the boundary composition. We report the angles between the traverses and the three crystallographic axis (α , β , γ) and the discrepancy value (in percentage). The analytical errors are ± 0.2 for the Fo (mol%), ± 0.02 for the NiO (wt%), ± 0.008 for the CaO (wt%), and ± 0.001 for the P (mol%). $\Delta(-)$ and $\Delta(+)$ are the errors on the total time calculated by DIPRA after the anisotropy correction.

^a Timescales have been calculated considering a homogeneous profile and constant composition; a step-like modeling would give times about 50% shorter. Sample nomenclature is as follows: 1) CM- and 251- refer to the pre- and post-caldera samples; 2) numbers after the hyphen refer to the crystal, and 3) melt inclusions have been designated with letters (e.g. CM-2-a is the melt inclusion a in the olivine 2 of the sample CM). The temperatures and fO_2 values for the modeling were chosen according to the values calculated from the olivine MIs. Both correspond to the averages for the two populations of MIs.

H₂O). We discuss the validity of this assumption in Section 4.4. We have modeled the water loss via H⁺ diffusion to test whether the D/H ratios (δD) versus H₂O content in our samples from the pre- and post-caldera eruptions can be explained by a dehydration process. We have considered an average melt inclusion with a radius of 50 μm hosted in an average spherical crystal with a radius of 500 μm , a temperature of 1160 °C, an initial concentration of H₂O that varies from 1 to 1.3 wt%, and an initial $\delta D = -100\%$.

3.5. H₂O degassing

In addition to H⁺ diffusive re-equilibration, both the water content and the hydrogen isotopic signature of the melt can also be affected by melt degassing. We have addressed this by modeling the variations of δD under closed (equation (1)) and open-system (equation (2)) conditions (Taylor, 1986):

$$\delta D_{melt} = \delta D_i - (1 - F)1000 \ln \alpha \quad (1)$$

$$\delta D_{melt} = \delta D_i - (1000 + \delta D_i)(1 - F^{\alpha-1}) \quad (2)$$

where δD_i is the initial composition of the melt, and F is the fraction of water remaining dissolved in the melt. We have calculated the fractionation factor α according to De Hoog et al. (2009). As initial magma composition we have considered the sample REU091110_DM-CM15 from Di Muro et al. (2014).

4. Results

4.1. Zoning patterns of olivine crystals

Olivine crystals from the early tephra emitted before caldera collapse (CM-samples) and from the post-caldera collapse lava (251-samples) display similar compositions and zoning patterns (Fig. 1; and Supplementary Material Fig. 1), with Fo [Fo = $100 \times \text{Mg}/(\text{Mg} + \text{Fe})$] values ranging from about 82 to about 86 (Table 1). BSE (Back-scattered Electron) images, X-Ray compositional maps, and EPMA traverses of phenocrysts show a slight reverse zoning (increase of about 1 mol% Fo) in the central part of crystals, with plateaus at Fo \approx 84–85 and at Fo \approx 85–86, followed by normal zoning towards the rim (Fo \approx 82–83; Fig. 1). Olivine in the vicinity of melt inclusions may show a compositional halo that is normally zoned towards the melt inclusion, with similar Fo to that of the crystal rims (Fig. 1c, f and g). Ni follows the zoning patterns of Fo, whereas Ca is typically a mirror image of Fo (Fig. 2a). The 2D Fe–Mg compositional maps around melt inclusions show zoning (Fig. 2d and f) that is in accord with the Fe–Mg diffusion anisotropy (see also below). 2D X-Ray maps of phosphorous (Fig. 1d and h) show complex zoning patterns which have been interpreted as an early episode of fast skeletal growth (Welsch et al., 2014) that lead to trapping of the melt inclusions (e.g. Manzini et al., 2017; Ruth et al., 2018). We measured a few profiles across the P-rich bands (e.g. Fig. 1h and 2g), which are S-shaped and have concentrations between about 0.01 and <0.005 mol% P. It is worth noting that crystal rims and composi-

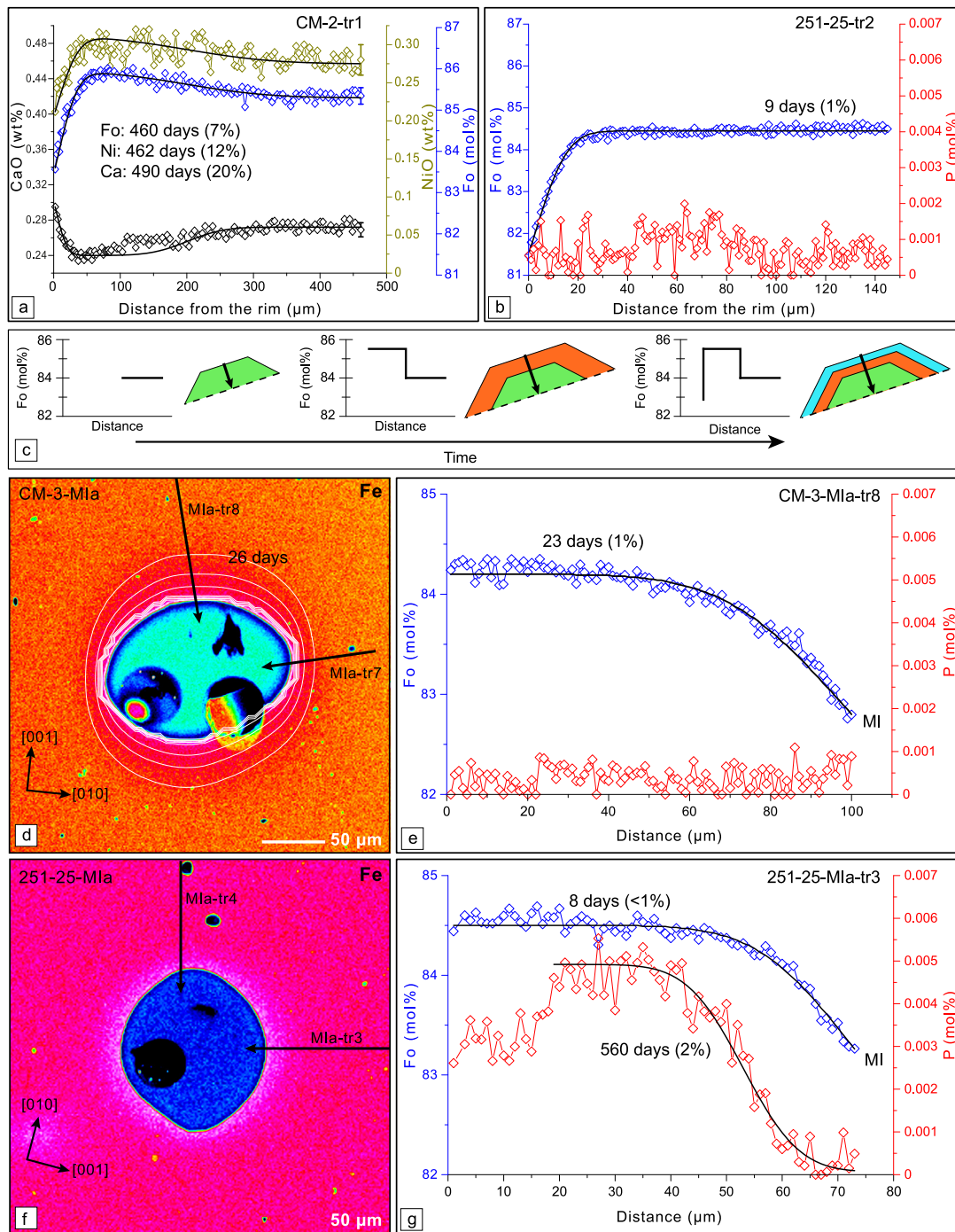


Fig. 2. Representative compositional profiles in olivine for Fo (mol%), CaO (wt%), NiO (wt%) and P (mol%) measured from rim to core in olivine crystals (a, b) and around melt inclusions (d, e, f, g). Timescales calculated using diffusion models are reported for each profile. Black lines are the best-fit diffusion models computed using DIPRA (step-like and homogeneous profile modeling for the reverse and normal zoning respectively). Numbers in parentheses indicate the discrepancy of the fit. **a**) Although the timescales for the three elements are similar, the large discrepancy obtained for Ca suggest that these profiles are affected by crystal growth, thus the time may be overestimated. **b**) Representative Fo and P profiles at the rim of the crystals. **c**) Conceptual approach used for modeling the zoning patterns: step function for the reverse zoning in the crystal core, and homogeneous profile and constant composition at the rim. **d**) Fe X-Ray compositional map and two-dimensional diffusion model (white lines show increasing diffusion times; see Supplementary Material Fig. 2). Crystallographic axes directions are also shown. The anisotropy effect is apparent, and the composition can be reproduced by a diffusion model (for 26 days). **e**) Fo and P profiles from traverses shown in d). Note that the one- and two-dimensional models give very similar times. **f**) As in d), the anisotropic Fe zoning can be observed. **g**) P displays a S-shaped profile and gives longer times that Fo probably due to significant contribution of growth zoning.

tional haloes around melt inclusion record only normal Fo zoning, and that the zoning patterns did not change during the eruption despite the changes in crystallinity. This suggests that the crystals are simply recording magma transport towards the surface (mainly lateral) rather than magma mixing or open system behavior in the magma plumbing system. Modeling the interface

between the olivine and the melt inclusion is an independent test for retrieving the thermal history of the crystals. The similarity of the crystal rim and the melt inclusion-haloes zoning patterns is key to support the magma transport hypothesis versus magma mixing, and therefore we have also modeled these diffusion profiles.

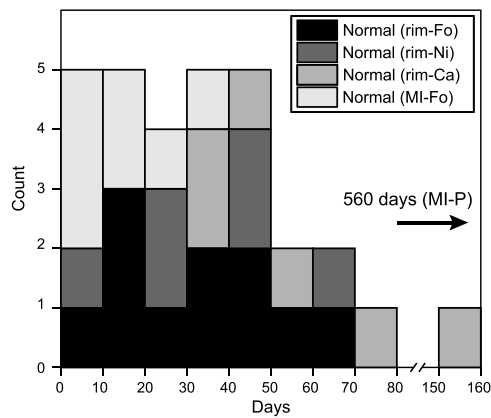


Fig. 3. Frequency histogram displaying the distribution of the calculated timescales for different elements (Fe–Mg, Ni, Ca and P) in olivine crystal rims and at the interface with melt inclusions.

4.2. Timescales recorded by olivine crystals and melt inclusions

Representative crystals were selected for modeling the concentration profiles and to calculate the timescales according to chemical diffusion. This includes crystals with reverse zoning at the core and normal zoning at the rims and towards the melt inclusions (Fig. 2). Diffusion modeling of reversely zoned Fo in the central part of the crystals yields good fits with low discrepancy values (Fig. 2a) and relatively long times of two to three years. However, the Ca and Ni fits generally have discrepancies close to 20% (Fig. 2a), which indicates that their shapes are not well explained by simple diffusion (Table 1). Moreover, visual inspection of the compositional gradients for Fo, Ni, Ca shows that they are all of about the same length, which should not be the case if diffusion was the only controlling factor given that they have different diffusivities. These observations make us think that a significant part of the reverse zoning profile could be due to growth, and thus that our times are overestimates of the real time. We also note that the reverse Fo zoning involves less than 1 mol% and thus could be explained by relatively small changes of melt composition, temperature or oxygen fugacity rather than mixing of different magmas from different storage regions (e.g. Pankhurst et al., 2018).

Modeling of Fo, Ni and Ca zoning towards the crystal rims, and near the melt inclusion margins, give a consistent answer (Fig. 2), with low discrepancy values and times ranging from about 3 to 157 days (Fig. 3), although the majority of times (82%) are less than two months (Table 1). Olivine crystals from the late-erupted lava give timescales slightly shorter than the pre-caldera samples (Table 1). Normal zoning of the Fo concentration towards the in-

terface between the olivine and the melt inclusion for the pre- and post-caldera samples (including the 2D model) (Fig. 2; Supplementary Materials Fig. 2) give timescales of about 2 to 30 days (Table 1), and overlap with those of the crystal rims.

The normal zoning towards the rim and around melt inclusions could be due to a drop in temperature and/or water content while in transport towards the surface. For example, MELTS (Ghiorso and Sack, 1995) simulations show that a decrease of 10–15 °C decreases 1 mol% Fo. Moreover, since the timescales calculated for the pre- and post-caldera olivine are similar, the process leading to the generation of the normal zoning in the olivine crystals is unlikely to be due to a pre-eruptive process in the reservoir. In that case, the late erupted post-caldera crystals should record about a month longer residence time. Our timescales support the hypothesis that the zoning is the result of the lateral transport from the mush zone to the vent in response to the change of environmental conditions.

We have also modeled one P profile (Figs. 1 and 2) at the interface between the olivine and a melt inclusion, and this yields a time of almost two years (Table 1). However, it is unclear if the full profile is due solely to diffusion. The halo of low P concentration around the melt inclusion (Fig. 1h) could reflect a more complex process of dissolution and crystallization (Manzini et al., 2017; Schiano et al., 2006) and might be revealing the extent of post-entrapment crystallization. Therefore, the times obtained from P are likely to be a maximum.

4.3. Volatile contents and δD of melt inclusions

The H₂O and CO₂ contents of the melt inclusions (Table 2) range from 0.6–1.1 wt% and 53 to 125 ppm, respectively, for the pre-caldera tephra, and from 0.32–0.82 wt% and 56 to 205 ppm for the post-caldera lava (Di Muro et al., 2014). These concentrations correspond to low saturation pressures (<0.5–0.4 kbar; Table 2; Fig. 4). The melt inclusions from the pre-caldera samples yield, on average, higher volatile saturation pressure, with respect to most post-caldera melt inclusions. Di Muro et al. (2014) calculated an average saturation pressure of 270 bar for the 2007 eruption using the Newman and Lowenstern (2002) model, slightly higher than the new average (250 bar) estimated using the Papale et al. (2006) model. As already shown by Di Muro et al. (2016), the two models provide very similar results in the pressure range <1 kbar typically recorded by melt inclusions in Pdf oceanites. Average pressure calculated using both models corresponds to a lithostatic depth range of 1280–1100 m below the volcano summit (ca. 1.5 km above sea level) considering a linear density increase from 1600 to 3400 kg m⁻³ (Di Muro et al., 2014). The maximum pressure recorded by the 2007 melt inclusion dataset is consistent with magma stor-

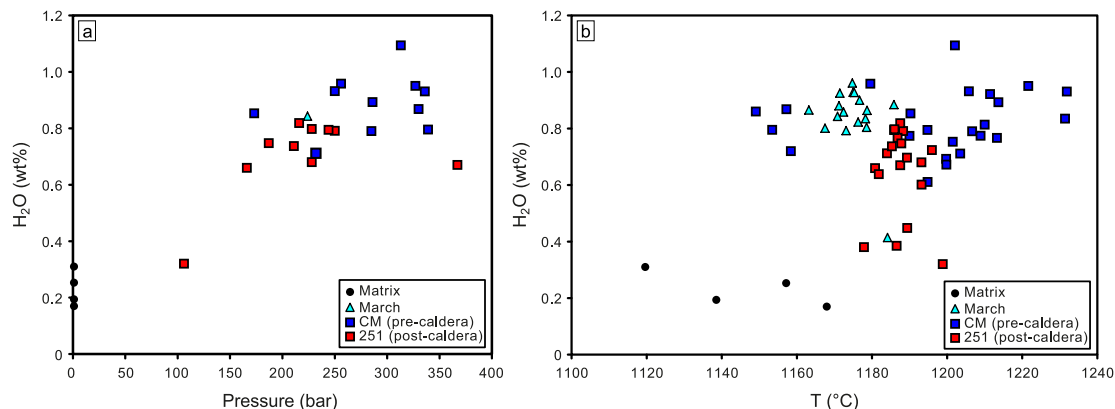


Fig. 4. Volatile saturation pressures (H₂O–CO₂; Papale et al., 2006) calculated for olivine hosted melt inclusions from eruptive products of the March 2007, pre- and post-caldera eruptions (April 2007). Olivine–melt equilibrium temperatures have been calculated using the Helz and Thornber (1987) MgO geothermometer (error $\pm 10^\circ\text{C}$).

Table 2
 δD (‰), water content (wt%; error of $\pm 9\%$) and CO_2 (ppm; error of $\pm 10\%$).

Sample-crystal	MI	Pre-caldera samples					Depth	Sample-crystal	MI	Post-caldera samples					Depth
		δD	δD error	H_2O	CO_2	P				δD	δD error	H_2O	CO_2	P	
CM-2	a			0.93	94	336	1683	251-4	a			0.64			
CM-2	b			0.72				251-6	a			0.71			
CM-3	a	-39	7	0.87	104	330	1653	251-8	a			0.38			
CM-4	a	-10	7	0.84				251-11	a			0.45			
CM-4	b	-47	5	0.79	86	285	1427	251-14	a			0.38			
CM-4	c			0.67				251-15	a	-51	7	0.8	75	228	1137
CM-5	b			0.86				251-16	a	-7	6	0.75	79	187	927
CM-17	a			0.75				251-16	b	-22	6	0.79	89	244	1219
CM-17	b			0.61				251-17	a	11	7	0.72			
CM-27	a			0.81				251-17	d	62	8	0.6			
CM-29	a			0.77				251-19	a	-63	6	0.79	133	250	1249
CM-29	b			0.79				251-20	a	-23	7	0.7			
CM-30	a			0.92				251-20	b	-77	6	0.68	114	228	1137
CM-30	b			0.69				251-22	a	-36	6	0.74	75	211	1050
CM-35	a	-115	5	0.71	94	232	1158	251-22	c	22	7	0.77			
CM-36	a	-85	6	0.96	104	256	1280	251-22	h	-51	7	0.82	74	216	1076
CM-36	b	-102	4	0.77				251-24	b			0.32	56	106	506
CM-39	a	-110	4			113		251-24	c	-11	7	0.66	60	166	818
CM-39	b	-135	5	1.09	101	313	1567	251-25	a	-30	6	0.67	204	367	1837
CM-40	a	-104	4	0.95	111	327	1638								
CM-40	b					95									
CM-43	a	-119	7	0.85	53	173	855								
CM-44	a	-103	6	0.93	76	250	1249								
CM-45	a	-108	4	0.89	99	286	1432								
CM-46	c			0.8	124	339	1697								

H_2O , CO_2 , saturations pressures and depth data from Di Muro et al. (2014). Saturation pressure (P) in bars and calculated corresponding depth below the crater in meters. Major element composition, diameter and the presence or not of a vapor bubble for each melt inclusion can be found in the supplementary material.

age slightly above the sea level, but most melt inclusions record lower pressure/trapping depth. Pre- and post-caldera melt inclusions have distinct temperature ranges. Temperatures calculated for post-entrapment crystallization show a larger range (1145 to 1232 °C) in pre-caldera samples, compared to post-caldera melt inclusions (1178 to 1199 °C; Fig. 4b). Di Muro et al. (2014) stress that the high-temperature range (>1200 °C) is inconsistent with the low average Fo content in olivine and the relatively evolved composition of aphyric lavas and glassy matrix melts. The lowest average temperature is recorded by melt inclusions in the early erupted cotectic basalts of March 2007 (1186–1134 °C). These

more evolved and cooler melts are also more degassed. A marked drop in dissolved water content (0.3 wt% < H_2O < 0.5 wt%) at constant temperature is recorded in some melt inclusions of the post caldera phase. On the contrary, melt inclusions of the pre-caldera phase having experienced marked post-entrapment modification do not show significant water loss.

The δD of melt inclusions varies from -135 to -10.3‰ and -77 to 62‰, for the pre- and post-caldera samples, respectively (Table 2). The pre-caldera melt inclusions display only a slight decrease in δD with the decrease of water (with the exception of three melt inclusions). In contrast, the post-caldera melt inclusions

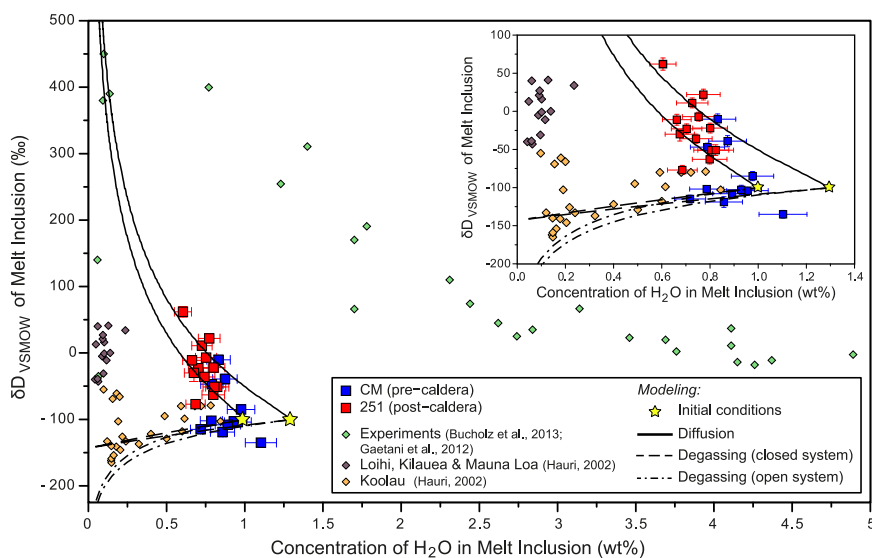


Fig. 5. Hydrogen-isotope fractionation (δD) versus dissolved water contents (relative error of $\pm 9\%$) in the olivine hosted melt inclusions from the pre- (blue squares) and post-caldera (red squares) phases of the April 2007 Piton de la Fournaise eruption. Solid curves are diffusion models calculated from an initial composition of $H_2O = 1-1.3$ wt% and $\delta D = -100$ ‰ (yellow stars). The diffusion models were computed with the following parameters: D calculated at 1160° parallel to [001], $k = 0.001$, $\beta = 0.3$ (Bucholz et al., 2013), $a = 50 \mu m$, $b = 500 \mu m$ (a and b are average values from Table 3). Diffusion parallel to [100] and [010] gives lower water contents. Dotted curves are the degassing models for the same initial conditions (closed and open). Most pre-caldera samples follow a general degassing trend, while post-caldera melt inclusions record variable degrees of H^+ diffusion.

Table 3
Timescales calculated from the H⁺ diffusion in melt inclusions through the olivine crystals.

Sample-crystal	MI	a (μm)	b (μm)	α	ϕ (%)	Time in days	
						$D = 1.6 \times 10^{-11} \text{ m}^2/\text{s}$ ([001])	$D = 1.2 \times 10^{-12} \text{ m}^2/\text{s}$ ([100], [010])
CM-3	a	63	438	0.144	19–43	0.1–0.4 (6.3)	2.2–5.4 (85)
CM-2	a	50	543	0.092	10–37	0.1–0.2 (4.3)	1.1–3.3 (57)
251-17	a	53	467	0.114	39–57	0.3–0.4 (4.7)	3.6–6.0 (63)
251-17	d	40	600	0.067	57–70	0.3–0.4 (2.8)	3.9–5.4 (38)
251-20	a	130	520	0.250	43–60	1.4–2.3 (23)	19–32 (314)
251-20	b	41	353	0.116	44–61	0.2–0.3 (2.8)	2.5–3.9 (37)
251-22	a	54	462	0.116	37–56	0.2–0.4 (4.8)	3.5–5.9 (64)
251-25	a	45	550	0.082	47–63	0.3–0.4 (3.5)	3.6–5.4 (47)

a is the radius of the melt inclusions and b is the shortest distance to the crystal rim measured in the BSE images. α is the ratio between a and b . For the calculation of the re-equilibration degree (ϕ) of melt inclusions we have considered as initial range of dissolved water 1–1.3 H₂O wt% and a final equilibrium concentration of 0.3 wt% in agreement with Di Muro et al. (2014). We provide the times calculated for D parallel to [001], [100] and [010] axes at 1160 °C. The two timescales depend on the initial composition, and hence on the re-equilibration degree. The values in parentheses are the time required to achieve a $\phi = 100\%$. In addition to the inherent uncertainties of Qin et al. (1992) model, these calculations are assuming a constant H⁺ composition at the crystal boundary during magma ascent and neglecting the tridimensional geometry of the crystals and melt inclusions.

show a general increase in the D/H ratios when the H₂O concentration decreases (Fig. 5). We stress here that melt inclusions having experienced marked water depletion (H₂O < 0.5 wt%) have not been analyzed for their D/H composition. To explain the variation in H₂O content, δD and CO₂ we have considered two possible end-member scenarios (see section 5.2).

4.4. Timescales of H₂O loss via diffusion

We have calculated the H₂O diffusive re-equilibration timescales for a wide range of parameter values and sizes. Although the re-equilibration degree varies significantly, (between 10 and 70%; Table 3), independently of the size or distance to the crystal rim of each melt inclusion, the timescales between different melt inclusions are similar. This suggests that our assumptions about treating all melt inclusions with a similar initial and equilibrium values are likely to be appropriated. The timescales calculated with diffusion parallel [001] are of a few hours, and those parallel to [100] and [010] are between one and six days (Supplementary Material Fig. 3). The only exception is the 251-20a melt inclusion, with a radius around three times bigger than the rest and connected by a fracture (Supplementary Material Fig. 1b and c).

5. Discussion

5.1. Magmatic processes recorded by the olivine crystals and their melt inclusions

Our results support the existence of different magma pockets below the PdF summit. The occurrence of a multilevel magma storage system is consistent with the presence of various seismic low-velocity zones below the cone of PdF (e.g. Prôno et al., 2009). Magmas erupted in February, March, and April 2007 have distinct Sr isotopic signatures. Olivine and melt inclusion compositions of March cotectic basalt are consistent with the eruption of a small volume of relatively evolved melt with a temperature of ca. 1160 °C. (Fig. 4b; Di Muro et al., 2014). The sudden and rapid isotopic shift recorded in lavas emitted at the beginning of caldera collapse (lowest value in ⁸⁷Sr/⁸⁶Sr) has been interpreted by Di Muro et al. (2014) as the evidence of the new magmatic input that pressurized and led to eruption of melts located in the shallow (<0.5 kbar) plumbing system. The crystal-rich lavas erupted after April 5th contain olivine with variable isotopic compositions (see Di Muro et al., 2014). However, we stress that isotopic data have been acquired on a large range of crystal sizes (from cm to mm), while crystal zoning and melt inclusion data discussed here concern the crystal size population <2 mm.

The relatively low Fo values of the olivine (86 to 82) from both, pre- and post-caldera eruptions, the absence of reverse Fo zoning near the rims, and the rarity of MgO-rich glass do not support a scenario of pre-eruptive mixing between a primitive deep magma and a shallow evolved one, as has been reported at other ocean island volcanoes (e.g. Albert et al., 2016). Another possibility is that the intruding melts were relatively evolved (MgO < 8 wt%) and interacted with a more mafic crystal pile left over from previous eruptions. However, several observations make this possibility quite unlikely: (1) the Fo values and extent of zoning of the crystal rims and between melt inclusions and crystal interface are the same, (2) we do not find any crystals with evolved cores of similar compositions to the rims, and (3) the time scales obtained from P modeling show that the crystal cores could not have remained at magmatic temperatures for more than about 1.5 years. These observations are more consistent with the Fo zoning due to magma transport towards the surface rather than the classical view of mixing between a mafic melt and an evolved cumulate. The low volatile saturation pressures calculated from the melt inclusions indicate that the erupted magmas were stored at quite shallow depths (ca. 0.5 km a.s.l.). The combined observations of chemical zoning, timescales, and shallow entrapment depths of melt inclusions can be interpreted as intrusion of magma at shallow depth that grew Fo 84–86 crystals which would be in equilibrium with more magnesian melts than those erupted. Thus many of the olivine crystals in fact grew and trapped the melt inclusions during the time period since the beginning of unrest and the end of the eruption (e.g. about 3 months). The normal zoning towards the crystal rims and around the melt inclusions (e.g., Fo 82–83) is likely due to transport of the magma from the shallow reservoir located near sea level towards the surface. The lateral transport under Piton de la Fournaise have an associated change in depth of about 1.5 km, and this will generate a change in the magma intensive conditions (e.g. temperature and water loss). Such short times for creating olivine mushes are also consistent with the evidence of fast growth provided by the fine P skeletal zoning (Welsch et al., 2014; this paper). However, given the limited size of our dataset we cannot fully discard the possibility that cumulates contain some crystals recycled from previous events, as suggested by the Sr isotopic differences between the olivine separates and the bulk-rock. These older cumulates are likely represented in the crystal populations larger than those examined in this study.

5.2. Entrapment of melt inclusions, degassing and depressurization of the system

The melt inclusions from the pre- and post-caldera samples display two different trends of water content vs. δD (Fig. 5). We

have considered two end-member scenarios for the interpretation of these variations. For both cases we first assume that the post-eruptive diffusive modification has not played a major role (e.g. Lloyd et al., 2013). This assumption is appropriated since we did not analyze inclusions with very low (<0.45 wt%) water content.

One end-member scenario is that the melt inclusions are trapped at different depths during magma ascent without diffusive re-equilibration, and the variations of water and δD follow as closed system evolution. This possibility has been considered before to explain the trend of samples from Koolau basalts from Hawaii (Hauri, 2002). Degassing will generate lower values of δD with decreasing water content (e.g. Bouvier et al., 2010), and the pre-caldera melt inclusions follow the degassing trends that we have calculated (Fig. 5). The CO_2 and S variation recorded in the melt inclusions also suggests a degassing trend (for further details see Di Muro et al., 2014).

The other end-member scenario is that the H_2O and δD variation is due to diffusive loss H^+ from melt inclusions that were trapped at the same depth, e.g. limited role for magma degassing. During magma ascent the melt inclusions would have experienced a progressive diffusive re-equilibration with the external surrounding and more degassed melt. The general increase in δD with the decrease of H_2O in the post-caldera samples suggests diffusive re-equilibration between the melt inclusions and the external melt through the olivine. In this case, the variation in the melt inclusions H_2O content and δD is related to the re-equilibration degree, which depends on the melt inclusion size and position inside the crystal. We have modeled the changes in the δD during dehydration from the initial conditions (Fig. 5). Once the H_2O re-equilibration degree (ϕ) of each melt inclusion has been estimated, the corresponding times can be calculated (see section 3.4).

Most of the H_2O and δD values of the pre-caldera melt inclusions fall into a magma degassing trend, whereas those of the post-caldera samples agree with a H^+ diffusion loss scenario (Fig. 5). If our initial water and δD are not correct, and were instead 1.5–2 wt% and to -150 to -200% , respectively, we could fit all samples with a single diffusive re-equilibration trend. Such low initial δD are unlikely because there is no evidence of crust recycling or dehydrated mantle in the PdF mantle source (Valer et al., 2017). Moreover, maximum dissolved water content documented in PdF magmas is rarely > 1.3 wt% (Di Muro et al., 2016). Another possibility is that the melt inclusions have experienced post-eruptive H^+ diffusion either during lava emplacement or after water quenching (e.g. Lloyd et al., 2013). This population is most likely represented by melt inclusions with a very low water content (<0.5 wt%), close to that of the matrix (0.3–0.2 wt%) and recording a very low apparent trapping pressure ($P < 150$ bar) (see supplementary material). Finally, depressurization of the magma pockets due to the caldera collapse and the sliding of the volcano flank could have promoted H^+ diffusive re-equilibration at depth before magma movement towards the surface started. The occurrence of two different trends (degassing and H^+ diffusion) is consistent with the results of Di Muro et al. (2014) who suggested that some of the melt inclusions experienced water loss based on the H_2O –S correlation. We do not find any correlation between the K_2O , CO_2 and H_2O content of the melt inclusions and therefore we have excluded the possibility of CO_2 fluxing (Métrich and Wallace, 2008; Supplementary Material Fig. 4). In conclusion, we suggest that lower pressures calculated for most (except for one melt inclusion) post-caldera melt inclusions with respect to pre-caldera samples result from post-entrapment partial H^+ loss.

The timescales calculated from the H^+ diffusive re-equilibration are very short compared with the Mg/Fe, Ni and Ca timescales. We interpret these timescales as records of the magma depressurization due to the flank sliding and the caldera collapse rather than magma movement towards the surface. This would explain why

the H^+ diffusive re-equilibration is mainly recorded by the post-caldera melt inclusions, even if some pre-caldera melt inclusions may be also recording the depressurization generated by flank sliding. According to Di Muro et al. (2014) the collapse of a 340 m deep caldera corresponds to a ca. 10 MPa depressurization. This value is consistent with the difference between the pressures calculated for the pre- and post-caldera melt inclusions and gives additional support to our interpretation that the lower H^+ values of post-caldera samples may reflect fast re-equilibration due to unloading and caldera collapse (Fig. 4). However, given that the post-caldera samples are lavas, we can't fully discard the possibility that water and δD for these samples has been partially affected by degassing on the Earth's surface.

5.3. Integration of petrological with monitoring data and sequence of events preceding and during the 2007 eruption

The timescales of magma transfer, H^+ loss, and magma storage depth that we have found can be used to better understand the monitoring data associated with this eruption (e.g. Albert et al., 2016, 2015; Kahl et al., 2011; Rasmussen et al., 2018). For the interpretation we have considered together the chemical zoning in olivine crystals, the diffusion modeling timescales, the geochemical data (whole rock compositions) and the geodetical data (Fig. 6).

Combination of the monitoring and petrologic data suggests that the new input of magma responsible of the edifice inflation (Fontaine et al., 2014) was located at 3 km b.s.l., but, intruded the shallow magmatic system and triggered the eruption of two shallow magma pockets (the February and March events) but did not interact with them, given their different Sr isotopic compositions. The lavas of these early eruptions are either aphyric (February) or contain rare iron-rich olivine (Fo 81–82; March) (Di Muro et al., 2014, 2016). This was followed by extensive and fast crystallization of olivine (Fo 82–86) and the lateral propagation of a sill from a crystal mush (April eruption). According to Froger et al. (2015), the crystal-rich magma would have encountered a pre-existing structural discontinuity, probably compensating for the lack of buoyancy due to the high crystal cargo and triggering a lateral eruption, in contrast with the mainly aphyric basalts from the early summit eruptions. Interestingly, caldera collapse was preceded by the increase in the lava crystal content, suggesting that displacement of the crystal mush contributed to volume changes leading to caldera foundering (Di Muro et al., 2014).

The sequence of processes preceding and during the 2007 eruption obtained from combining monitoring, crystal, and melt inclusion information can be explained with the following stages (please see Figs. 6 and 7): (1) In January, inflation started due to new magma intrusion at depth (ca. 3 km b.s.l.) followed by magma movement to the shallow plumbing system (ca. 0.5 km a.s.l.), pressurizing pre-existing magma pockets that moved towards the surface in January. This is consistent with a progressive increase in shallow microseismicity below the volcano summit in January and early February (OVPF unpublished data). This early magma movement is recorded in the crystal timescales (normal zoning; Fig. 6c). (2) In February aphyric basalts with high $^{87}Sr/^{86}Sr$ were erupted. Pressurization continued, and olivine records that the pre-caldera magma kept moving towards the surface. (3) March is a period of non-inflation culminating with a sudden flank sliding, and it might correspond to continuous lateral transport of a newly created crystal mush in response to the underlying pressurization. (4) At the end of March, the second eruption took place. The cotectic basalts are evolved and have isotopic compositions different to the February eruption, which suggest they are derived from a different magma pocket (Di Muro et al., 2014). The lateral transport from the crystal mush continues. (5) On April 2nd the distal main eruptive phase starts with the emission of aphyric basalts,

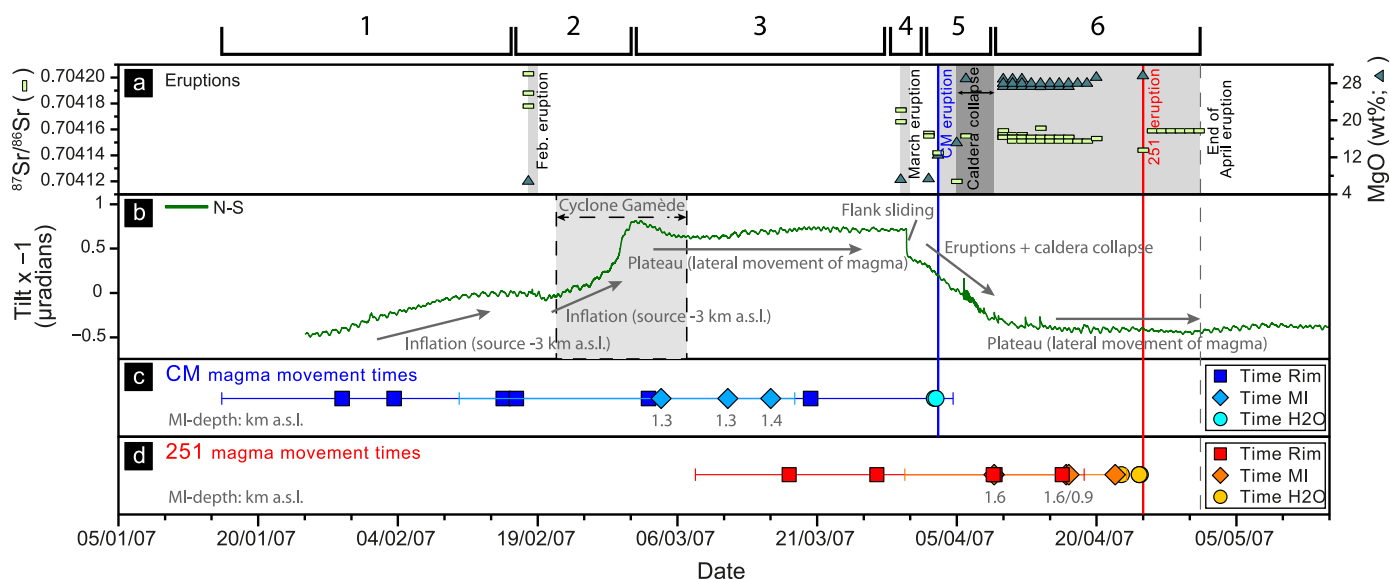


Fig. 6. Correlation between the olivine and melt inclusions timescales with the geochemical and geophysical data. The numbers above the first panel correspond to the numbers in the main text (Section 5.3). **a)** The duration of the eruptions is represented by light grey bands. The onset of the pre- and post-caldera eruptions is marked with a blue and a red line, respectively. The caldera collapse event is represented with a dark grey band. **b)** Inflation-deflation cycle and correlation with geological events. **c, d)** Timescales calculated from modeling the diffusion of Fe–Mg in the pre- and post-caldera olivine crystals (error bars include NiO and CaO data when available) and of H₂O in melt inclusions. Timescales are plotted from the eruption dates (3 and 25 April 2007), as detailed in the main text (sections 4.3 and 4.4). The different timescales between crystals likely reflect the range of transport times from the crystal-mush to the surface.

and on April 3rd the pre-caldera collapse olivine basalts (CM samples) erupt. The water and δD values of melt inclusions mainly record magma degassing (Fig. 5) over a shallow pressure range. The timescales of olivine crystals indicate that the magmas that yield the post-caldera eruption already started to move towards the surface (Fig. 6d). Two days later, on April 5th the caldera started to collapse. (6) During April the olivine crystals record timescales that suggest magma kept moving after the collapse. Our post-caldera collapse samples (oceanites; 251 samples) were erupted on April 25th. The melt inclusions hosted by the olivine crystals mainly record H⁺ loss via diffusion due to the depressurization related to caldera collapse and flank sliding (Fig. 5) or degassing on the Earth's surface due to slow quenching of the samples.

6. A role for the magma flux in the architecture of volcanic plumbing systems?

Piton de la Fournaise and Kilauea are intraplate basaltic volcanoes associated with a mantle plume of high activity, and both volcanoes have well-developed shallow magma ponding zones (e.g. Prôno et al., 2009; Sides et al., 2014). However, in contrast with our findings at PdF, magmas erupted from Kilauea during inflation periods reflect mixing between the new input and the shallow reservoir (Lynn et al., 2017; Poland et al., 2012; Sides et al., 2014). Studies of Mt. Etna olivine crystals also show evidence of multiple mixing episodes preceding the eruption (e.g. Kahl et al., 2011), which may reflect a plumbing system made of multiple but well-connected reservoirs due to the high magma flux at this volcano (Kahl et al., 2011). Mafic ocean island volcanoes with lower magma supply rates as the Canary Islands (e.g. Tenerife, El Hierro and La Palma) also display evidence of magma mixing recorded in olivine (e.g. Albert et al., 2015; Klügel et al., 2005). During the El Hierro 2011 eruption, the geophysical monitoring data indicated similar depths to those calculated by geochemical methods, and also evidence for mixing between a shallow evolved melt and a deeper more primitive melt recorded in the olivine crystals (Longpré et al., 2014; López et al., 2012).

The different behavior of these systems may be related to their different magma supply rate (e.g. White et al., 2006) and plumbing system architecture. At one end of the spectrum we have the case of high magma flux systems such as Kilauea and Etna, with a plumbing system characterized by open paths and well-connected reservoirs facilitating the interaction between any new intruding melts and those that resided in various pockets. At the other end, we have much less active systems like the Canary Islands where eruptions are mainly driven by dykes. Magma mixing and interactions between resident and intruding magmas are also recorded, but in this case they may be necessary for opening a path towards the surface and allowing the magmas to erupt (Albert et al., 2016). In this scenario, dykes that do not intercept previously emplaced magma pockets may result in failed eruptions. Pdf volcano may be somewhere between these two end members: intruding melts at depth are able to trigger eruptions by mobilizing shallower isolated melt pockets, although they can also bypass them. This may be possible because the shallow pockets may still be relatively well connected to the surface and can erupt. Pdf may be an example of a high magma flux system, as Kilauea or Etna, but in which the plumbing system connections between shallow pockets and deep conduits are not necessarily active. More studies that contrast the depths and magmatic processes inferred from monitoring networks with those obtained from crystals and host melt inclusions should be able to clarify the different architecture of volcanic systems according to magmatic fluxes and hopefully improve hazard mitigation strategies of associated eruptions.

7. Conclusions

The olivine crystals and melt inclusions from the 2007 Pdf eruption record shallow storage depth and re-equilibration related to lateral magma movement towards the surface. Most crystals we have studied likely grew during the pre-eruption and eruption period (e.g. in about 3 months) from the basalt that migrated from, and was temporarily stored at shallow depths (e.g. about 0.5 km a.s.l.), although deformation source modeled from tilt data indicates an initially deeper magma source (ca. 3 km b.s.l.). These

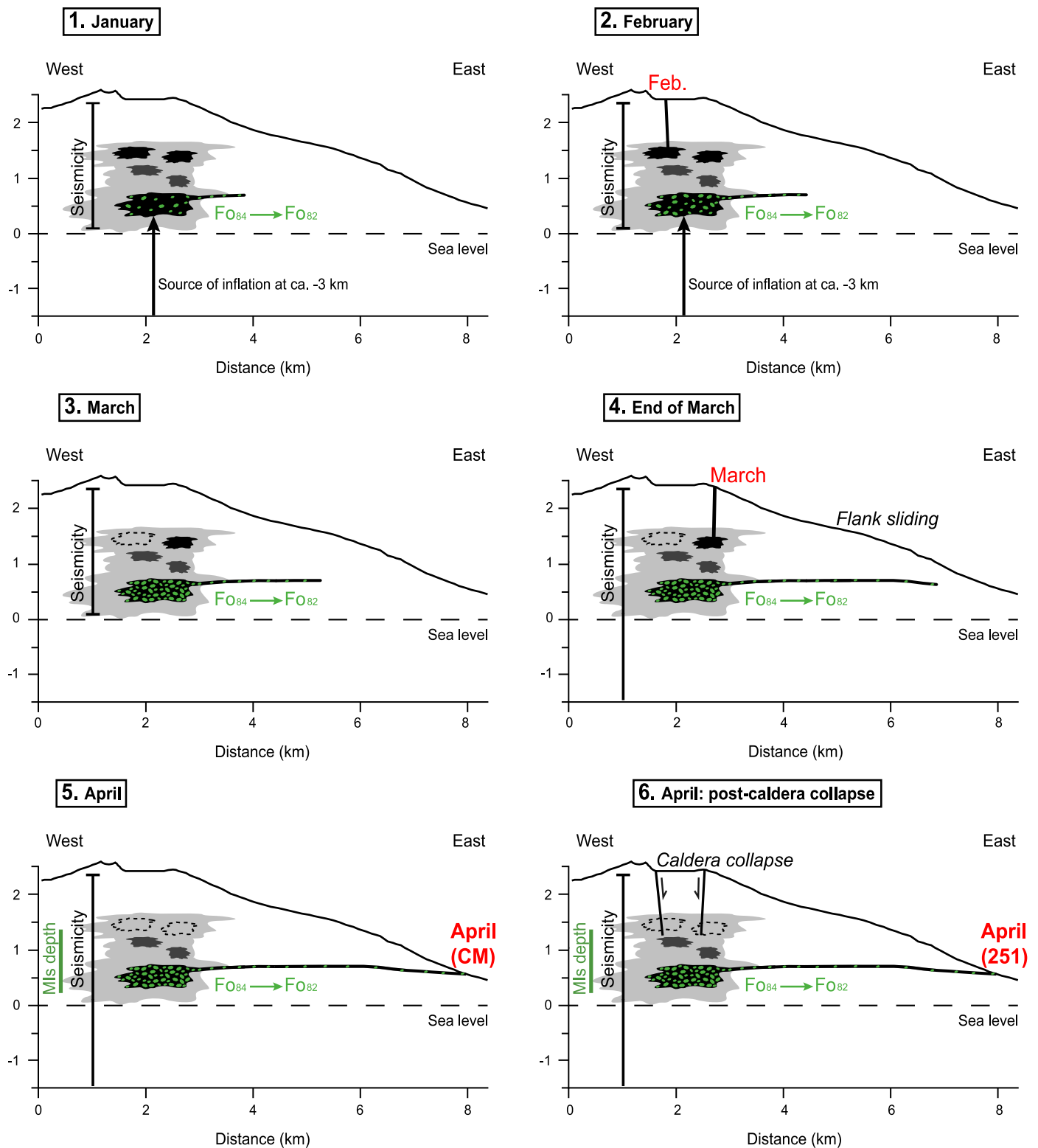


Fig. 7. Schematic model of the plumbing system processes preceding and during the 2007 eruption. For more details see main text (section 5.3).

observations suggest that magma arrival at shallow depth pressurized the pre-existing melts and led to eruption of aphyric magma, but we have no evidence of physical interaction between the two. The zoning and timescales derived from olivine crystals agree with fast crystal growth, creation of a crystal mush and subsequent lateral transport, eruption, and caldera collapse. Timescales deduced from Fe/Mg, Ni and Ca in olivine rims and towards melt inclusions are relatively short (from 3 to 60 days) and agree with the changes

in monitoring data. P zoning in the crystal interiors also indicates relatively short times (<1.5 years) between olivine crystallization and eruption. Degassing and re-equilibration of H^+ of melt inclusions via diffusion occurred during the depressurization of the shallow system and caldera collapse and vary between a few hours to six days (depending on the crystallographic direction). Our results on the dynamic of magmatic processes, vent locations, and magma transport have implications for similar large mafic ocean

island volcanoes such as Kilauea. However, the role of magma supply rates that we propose to shape the plumbing systems of these volcanoes should be further investigated by numerical or analogue experiments.

Acknowledgements

We thank F.R. Fontaine for sharing the tilt data and the OVPF for the data and sample collection. We are grateful for the discussion about surface deformation implications with C. Lopez, and about degassing modeling with J. De Hoog. We thank D. Rasmussen, an anonymous reviewer, and editor T. Mather for their contributions that helped much to improve the manuscript. H. Albert and F. Costa were supported by a National Research Foundation Investigatorship Award (grant number NRF-NRFI2017-06) from Singapore.

Appendix A. Supplementary material

Supplementary material related to this article can be found online at <https://doi.org/10.1016/j.epsl.2019.02.035>.

References

- Albert, H., Costa, F., Martí, J., 2016. Years to weeks of seismic unrest and magmatic intrusions precede monogenetic eruptions. *Geology* 44, 211–214. <https://doi.org/10.1130/G37239.1>.
- Albert, H., Costa, F., Martí, J., 2015. Timing of magmatic processes and unrest associated with mafic historical monogenetic eruptions in Tenerife Island. *J. Petrol.* 56, 1945–1966. <https://doi.org/10.1093/ptrology/egv058>.
- Bouvier, A.S., Métrich, N., Deloule, E., 2010. Light elements, volatiles, and stable isotopes in basaltic melt inclusions from Grenada, Lesser Antilles: inferences for magma genesis. *Geochem. Geophys. Geosyst.* 11, 1–20. <https://doi.org/10.1029/2010GC003051>.
- Bucholz, C.E., Gaetani, G.A., Behn, M.D., Shimizu, N., 2013. Post-entrapment modification of volatiles and oxygen fugacity in olivine-hosted melt inclusions. *Earth Planet. Sci. Lett.* 374, 145–155. <https://doi.org/10.1016/j.epsl.2013.05.033>.
- Cashman, K.V., Sparks, R.S.J., Blundy, J.D., 2017. Vertically extensive and unstable magmatic systems: a unified view of igneous processes. *Science* 355, 6331. <https://doi.org/10.1126/science.aag3055>.
- Chen, Y., Provost, A., Schiano, P., Cluzel, N., 2011. The rate of water loss from olivine-hosted melt inclusions. *Contrib. Mineral. Petrol.* 162, 625–636. <https://doi.org/10.1007/s00410-011-0616-5>.
- Collins, S.J., Pyle, D.M., MacLennan, J., 2009. Melt inclusions track pre-eruption storage and dehydration of magmas at Etna. *Geology* 37, 571–574. <https://doi.org/10.1130/G30040A.1>.
- Costa, F., Chakraborty, S., 2004. Decadal time gaps between mafic intrusion and silicic eruption obtained from chemical zoning patterns in olivine. *Earth Planet. Sci. Lett.* 227, 517–530. <https://doi.org/10.1016/j.epsl.2004.08.011>.
- Costa, F., Dohmen, R., Chakraborty, S., 2008. Time scales of magmatic processes from modeling the zoning patterns of crystals. *Rev. Mineral. Geochem.* 69, 545–594. <https://doi.org/10.2138/rmg.2008.69.14>.
- Costa, F., Dungan, M., 2005. Short time scales of magmatic assimilation from diffusion modeling of multiple elements in olivine. *Geology* 33, 837–840. <https://doi.org/10.1130/G21675.1>.
- Danyushevsky, L.V., Della-Pasqua, F.N., Sokolov, S., 2000. Re-equilibration of melt inclusions trapped by magnesian olivine phenocrysts from subduction-related magmas: petrological implications. *Contrib. Mineral. Petrol.* 138, 68–83. <https://doi.org/10.1007/PL00007664>.
- Danyushevsky, L.V., Leslie, R.A.J., Crawford, A.J., Durance, P., 2004. Melt inclusions in primitive olivine phenocrysts: the role of localized reaction processes in the origin of anomalous compositions. *J. Petrol.* 45, 2531–2553. <https://doi.org/10.1093/ptrology/egh080>.
- De Hoog, J.C.M., Taylor, B.E., Van Bergen, M.J., 2009. Hydrogen-isotope systematics in degassing basaltic magma and application to Indonesian arc basalts. *Chem. Geol.* 266, 265–275. <https://doi.org/10.1016/j.chemgeo.2009.06.010>.
- Di Muro, A., Métrich, N., Vergani, D., Rosi, M., Armienti, P., Fougeroux, T., Deloule, E., Arienzo, I., Civetta, L., 2014. The shallow plumbing system of Piton de la Fournaise Volcano (La Réunion Island, Indian Ocean) revealed by the major 2007 caldera-forming eruption. *J. Petrol.* 55, 1287–1315. <https://doi.org/10.1093/ptrology/egu025>.
- Di Muro, A., Métrich, N., Allard, P., Aiuppa, A., Burton, M., Galle, B., 2016. Magma degassing at Piton de la Fournaise Volcano. In: *Active Volcanoes of the Southwest Indian Ocean*. Springer, Berlin, Heidelberg, pp. 203–222.
- Fontaine, F.R., Roullet, G., Michon, L., Barruol, G., Di Muro, A., 2014. The 2007 eruptions and caldera collapse of the Piton de la Fournaise volcano (La Réunion Island) from tilt analysis at a single very broadband seismic station. *Geophys. Res. Lett.* 41, 2803–2811. <https://doi.org/10.1002/2014GL059691>.
- Frezza, M.L., 2001. Silicate-melt inclusions in magmatic rocks: applications to petrology. *Lithos* 55, 273–299. [https://doi.org/10.1016/S0024-4937\(00\)00048-7](https://doi.org/10.1016/S0024-4937(00)00048-7).
- Froger, J.L., Famin, V., Cayol, V., Augier, A., Michon, L., Lénat, J.F., 2015. Time-dependent displacements during and after the April 2007 eruption of Piton de la Fournaise, revealed by interferometric data. *J. Volcanol. Geotherm. Res.* 296, 55–68. <https://doi.org/10.1016/j.jvolgeores.2015.02.014>.
- Gaetani, G.A., O'Leary, J.A., Shimizu, N., Bucholz, C.E., Newville, M., 2012. Rapid re-equilibration of H₂O and oxygen fugacity in olivine-hosted melt inclusions. *Geology* 40, 915–918. <https://doi.org/10.1130/G32992.1>.
- Ghiorso, M.S., Sack, R.O., 1995. Chemical mass transfer in magmatic processes IV. A revised and internally consistent thermodynamic model for the interpolation and extrapolation of liquid-solid equilibria in magmatic systems at elevated temperatures and pressures. *Contrib. Mineral. Petrol.* 119, 197–212. <https://doi.org/10.1007/BF00307281>.
- Girona, T., Costa, F., 2013. DIPRA: a user-friendly program to model multi-element diffusion in olivine with applications to timescales of magmatic processes. *Geochem. Geophys. Geosyst.* 14, 422–431. <https://doi.org/10.1029/2012GC004427>.
- Hauri, E., 2002. SIMS analysis of volatiles in silicate glasses. 2: isotopes and abundances in Hawaiian melt inclusions. *Chem. Geol.* 183, 115–141. [https://doi.org/10.1016/S0009-2541\(01\)00374-6](https://doi.org/10.1016/S0009-2541(01)00374-6).
- Helz, R.T., Thornber, C.R., 1987. Geothermometry of Kilauea Iki lava lake, Hawaii. *Bull. Volcanol.* 49, 651–668.
- Kahl, M., Chakraborty, S., Costa, F., Pompilio, M., 2011. Dynamic plumbing system beneath volcanoes revealed by kinetic modeling, and the connection to monitoring data: an example from Mt. Etna. *Earth Planet. Sci. Lett.* 308, 11–22. <https://doi.org/10.1016/j.epsl.2011.05.008>.
- Klügel, A., Hansteen, T.H., Galipp, K., 2005. Magma storage and underplating beneath Cumbre Vieja volcano, La Palma (Canary Islands). *Earth Planet. Sci. Lett.* 236, 211–226. <https://doi.org/10.1016/j.epsl.2005.04.006>.
- Kress, V.C., Carmichael, I.S.E., 1991. The compressibility of silicate liquids containing Fe₂O₃ and the effect of composition, temperature, oxygen fugacity and pressure on their redox states. *Contrib. Mineral. Petrol.* 108, 82–92. <https://doi.org/10.1007/BF00307328>.
- Lloyd, A.S., Plank, T., Ruprecht, P., Hauri, E.H., Rose, W., 2013. Volatile loss from melt inclusions in pyroclasts of differing sizes. *Contrib. Mineral. Petrol.* 165, 129–153. <https://doi.org/10.1007/s00410-012-0800-2>.
- Longpré, M.A., Klügel, A., Diehl, A., Stix, J., 2014. Mixing in mantle magma reservoirs prior to and during the 2011–2012 eruption at El Hierro, Canary Islands. *Geology* 42, 315–318. <https://doi.org/10.1130/G35165.1>.
- López, C., Blanco, M.J., Abella, R., Brenes, B., Cabrera Rodríguez, V.M., Casas, B., Domínguez Cerdeña, I., Felpeo, A., De Villalta, M.F., Del Fresno, C., García, O., García-Arias, M.J., García-Cañada, L., Gomis Moreno, A., Gonzalez-Alonso, E., Guzmán Pérez, J., Iribarren, I., López-Díaz, R., Luengo-Oroz, N., Meletlidis, S., Moreno, M., Moure, D., De Pablo, J.P., Rodero, C., Romero, E., Sainz-Maza, S., Sente Domingo, M.A., Torres, P.A., Trigo, P., Villasante-Marcos, V., 2012. Monitoring the volcanic unrest of El Hierro (Canary Islands) before the onset of the 2011–2012 submarine eruption. *Geophys. Res. Lett.* 39, 1–7. <https://doi.org/10.1029/2012GL051846>.
- Lynn, K.J., García, M.O., Shea, T., Costa, F., Swanson, D.A., 2017. Timescales of mixing and storage for Keanakāko'i Tephra magmas (1500–1820 C.E.), Kīlauea Volcano, Hawai'i. *Contrib. Mineral. Petrol.* 172. <https://doi.org/10.1007/s00410-017-1395-4>.
- Manzini, M., Bouvier, A.S., Baumgartner, L.P., Müntener, O., Rose-Koga, E.F., Schiano, P., Escrig, S., Meibom, A., Shimizu, N., 2017. Weekly to monthly time scale of melt inclusion entrapment prior to eruption recorded by phosphorus distribution in olivine from mid-ocean ridges. *Geology* 45, 1059–1062. <https://doi.org/10.1130/G39463.1>.
- Métrich, N., Bertagnini, A., Di Muro, A., 2009. Conditions of magma storage, degassing and ascent at Stromboli: new insights into the volcano plumbing system with inferences on the eruptive dynamics. *J. Petrol.* 51, 603–626. <https://doi.org/10.1093/ptrology/egp083>.
- Métrich, N., Deloule, E., 2014. Water content, δD and $\delta^{11}B$ tracking in the Vanuatu arc magmas (Aoba Island): insights from olivine-hosted melt inclusions. *Lithos* 206–207, 400–408. <https://doi.org/10.1016/j.lithos.2014.08.011>.
- Métrich, N., Wallace, P.J., 2008. Volatile abundances in basaltic magmas and their degassing paths tracked by melt inclusions. *Rev. Mineral. Geochem.* 69, 363–402. <https://doi.org/10.2138/rmg.2008.69.10>.
- Michon, L., Staudacher, T., Ferrazzini, V., Bachèlery, P., Marti, J., 2007. April 2007 collapse of Piton de la Fournaise: a new example of caldera formation. *Geophys. Res. Lett.* 34, 1–6. <https://doi.org/10.1029/2007GL031248>.
- Newman, S., Lowenstern, J.B., 2002. VolatileCalc: a silicate melt–H₂O–CO₂ solution model written in Visual Basic for excel. *Comput. Geosci.* 28, 597–604. [https://doi.org/10.1016/S0098-3004\(01\)00081-4](https://doi.org/10.1016/S0098-3004(01)00081-4).
- Pankhurst, M.J., Morgan, D.J., Thordarson, T., Loughlin, S.C., 2018. Magmatic crystal records in time, space, and process, causatively linked with volcanic unrest. *Earth Planet. Sci. Lett.* 493, 231–241. <https://doi.org/10.1016/j.epsl.2018.04.025>.

- Papale, P., Moretti, R., Barbato, D., 2006. The compositional dependence of the saturation surface of H₂O + CO₂ fluids in silicate melts. *Chem. Geol.* 229, 78–95. <https://doi.org/10.1016/j.chemgeo.2006.01.013>.
- Peltier, A., Bachèlery, P., Staudacher, T., 2009. Magma transport and storage at Piton de La Fournaise (La Réunion) between 1972 and 2007: a review of geophysical and geochemical data. *J. Volcanol. Geotherm. Res.* 184, 93–108. <https://doi.org/10.1016/j.jvolgeores.2008.12.008>.
- Peltier, A., Beauducel, F., Villeneuve, N., Ferrazzini, V., Di Muro, A., Aiuppa, A., Derrien, A., Jourde, K., Taisne, B., 2016. Deep fluid transfer evidenced by surface deformation during the 2014–2015 unrest at Piton de la Fournaise volcano. *J. Volcanol. Geotherm. Res.* 321, 140–148. <https://doi.org/10.1016/j.jvolgeores.2016.04.031>.
- Poland, M.P., Miklius, A., Jeff Sutton, A., Thornber, C.R., 2012. A mantle-driven surge in magma supply to Kīlauea Volcano during 2003–2007. *Nat. Geosci.* 5, 295–300. <https://doi.org/10.1038/ngeo1426>.
- Prôno, E., Battaglia, J., Monteiller, V., Got, J.L., Ferrazzini, V., 2009. P-wave velocity structure of Piton de la Fournaise volcano deduced from seismic data recorded between 1996 and 1999. *J. Volcanol. Geotherm. Res.* 184, 49–62. <https://doi.org/10.1016/j.jvolgeores.2008.12.009>.
- Qin, Z., Lu, F., Anderson, A.T., 1992. Diffusive reequilibration of melt and fluid inclusions. *Am. Mineral.* 77, 565–576.
- Rasmussen, D.J., Plank, T.A., Roman, D.C., Power, J.A., Bodnar, R.J., Hauri, E.H., 2018. When does eruption run-up begin? Multidisciplinary insight from the 1999 eruption of Shishaldin volcano. *Earth Planet. Sci. Lett.* 486, 1–14. <https://doi.org/10.1016/j.epsl.2018.01.001>.
- Ruth, D.C.S., Costa, F., Bouvet de Maisonneuve, C., Franco, L., Cortés, J.A., Calder, E.S., 2018. Crystal and melt inclusion timescales reveal the evolution of magma migration before eruption. *Nat. Commun.* 9, 2657. <https://doi.org/10.1038/s41467-018-05086-8>.
- Schiano, P., Provost, A., Clocchiatti, R., Faure, F., 2006. Transcrystalline melt migration and Earth's mantle. *Science* 80 (314), 970–974. <https://doi.org/10.1126/science.1132485>.
- Shea, T., Costa, F., Krimer, D., Hammer, J.E., 2015. Accuracy of timescales retrieved from diffusion modeling in olivine: a 3D perspective. *Am. Mineral.* 100, 2026–2042. <https://doi.org/10.2138/am-2015-5163>.
- Sides, I.R., Edmonds, M., MacLennan, J., Swanson, D.A., Houghton, B.F., 2014. Eruption style at Kīlauea Volcano in Hawai'i linked to primary melt composition. *Nat. Geosci.* 7, 464–469. <https://doi.org/10.1038/ngeo2140>.
- Staudacher, T., Ferrazzini, V., Peltier, A., Kowalski, P., Boissier, P., Catherine, P., Lauret, F., Massin, F., 2009. The April 2007 eruption and the Dolomieu crater collapse, two major events at Piton de la Fournaise (La Réunion Island, Indian Ocean). *J. Volcanol. Geotherm. Res.* 184, 126–137. <https://doi.org/10.1016/j.jvolgeores.2008.11.005>.
- Taylor, B.E., 1986. Magmatic volatiles: isotopic variation of C, H and S. Stable isotopes in high temperature geological processes. In: Valley, J.W., Taylor, H.P., O'Neil, J.R. (Eds.), *Reviews in Mineralogy*, pp. 185–225.
- Valer, M., Schiano, P., Bachèlery, P., 2017. Geochemical characteristics of the La Réunion mantle plume source inferred from olivine-hosted melt inclusions from the adventive cones of Piton de la Fournaise volcano (La Réunion Island). *Contrib. Mineral. Petrol.* 172, 1–20. <https://doi.org/10.1007/s00410-017-1397-2>.
- Welsch, B., Hammer, J., Hellebrand, E., 2014. Phosphorus zoning reveals dendritic architecture of olivine. *Geology* 42, 867–870. <https://doi.org/10.1130/G35691.1>.
- White, S.C., Crisp, J.A., Spera, F.J., 2006. Long-term volumetric eruption rates and magma budgets. *Geochem. Geophys. Geosyst.* 7, Q03010. <https://doi.org/10.1029/2005GC001002>.